

# **On the dynamic assessment of the Local-Maximum Entropy Material Point Method through an Explicit Predictor-Corrector Scheme**

Miguel Molinos, Pedro Navas, Manuel Pastor and  
Miguel Martín-Stickle.

## **Highlights**

- We have proposed a A new **accurate** and efficient time integration scheme for the MPM is proposed. ~~in order to dissipate spurious stress oscillations without damping the solution.~~
- The proposal of the Local Maximum-Entropy (LME) approximation technique ~~under the~~ is a robust substitute of the traditional shape functions **within the** MPM framework .
- Our **The proposed approach might improve** have clear benefits on large strain fast dynamic MPM simulations ,~~where the grid-crossing pathology appears.~~ as grid-crossing pathology are clearly mitigated.

# On the dynamic assessment of the Local-Maximum Entropy Material Point Method through an Explicit Predictor-Corrector Scheme

Miguel Molinos<sup>a</sup>, Pedro Navas<sup>a1</sup>, Manuel Pastor<sup>a</sup> and Miguel Martín Stickle<sup>a</sup>

<sup>a</sup> *ETSI Caminos, Canales y Puertos, Universidad Politécnica de Madrid.  
c. Prof. Aranguren 3, 28040 Madrid, Spain*

---

## Abstract

Material Point Method (MPM) has arisen in the recent years as an alternative to Finite Element Method (FEM) under large **deformations**. However, the simulation of shock waves propagation in the large deformation regime is still challenging under this approach due to the incapability of the standard MPM time integration scheme to filter spurious noises. To overcome it, we propose in this paper an explicit Predictor-Corrector time integration scheme. Its powerful performance mitigates the presence of spurious oscillations with minimal dissipation in high frequency problems. Other source of numerical noise in MPM occurs when the material points cross computational grid boundaries, being caused by the lack of smoothness of the interpolation functions. This noise results in spurious local variations at the material points, where strain-stress fields are computed. This could lead to inaccurate solutions as well as aborted simulations in the worst cases. To surmount it, we propose in this work the Local Maximum-Entropy (LME) approximation schemes as a robust substitute of the traditional shape function in MPM. **The performance of both improvements is validated by the high quality results of the numerical examples.**

*Keywords:* LME, MPM, Explicit predictor-corrector, Dynamic problems

---

<sup>1</sup>Corresponding author: p.navas@upm.es

## 1. Introduction

Since the proposal of MPM by Sulusky *et al.* (1994) [1] as a generalization to solids of the Fluid Implicit Particle (FLIP) method [2], its popularity has increased due to its ability to deal with large strain regime without suffering  
5 mesh distortion inaccuracies. One of the main fields where this method is widely used is solid dynamics.

On one hand, the main source of instability occurs when material points cross cell boundaries. This issue led to the development of other interpolation techniques to overcome this limitation such as the Generalized Interpolation Material Point (GIMP) method Bardenhagen & Kober (2004) [3], which has demonstrated to have a good performance in the finite deformation regime. However, in the absence of a regular grid, construction of the weighting functions is only achieved at considerable effort and computational cost. Furthermore, as it is a voxel-based discretisation technique,  
10 it is prone to suffer voxel domains overlap or gaps when the material point mesh becomes irregular, which can introduce severe inaccuracies as noticed by Steffen *et al.* (2008)[4]. This is similar to the difficulty encountered by the finite element method due to element distortion. A more robust alternative is the Dual Domain Material Point (DDMP) method proposed by Zhang *et  
15 al.* (2011) [5]. Unfortunately this method shows an unsatisfactory behaviour when particle/cell ratio decreases. Therefore DDMP requires a large number of particles for convergence [6], what makes the method computationally expensive. To avoid tensile instabilities that are quite common in extension,  
20 Sadeghirad *et al.* (2011) [7] developed the CPDI [7]. In recent years, the employment of spline-lines as shape functions has gained popularity with the introduction of the B-Spline MPM proposed by Tielen *et al.* (2017) [8], in which unstructured set of nodes and particles can be considered. More recently, approximants derived from minimization have been introduced into  
25 the MPM framework with the Conservative Taylor Least Squares (CTLS)  
30 reconstruction proposed by Wobbes *et al.* (2018) [9]. Unfortunately, when particles are spread in some particular special patterns, the quality of the CTLS approximation decreases locally.

This document adopts the Local Maximum-Entropy (LME), or Local *Max-Ent* approximates, as a robust substitute of the aforementioned shape  
35 functions in MPM. First introduced by Arroyo & Ortiz (2006) [10], it belongs to the class of convex approximation schemes and provides a seamless transition between FEM and meshfree interpolations. The LME approximation is based on a compromise between minimizing the width of the shape function support and maximizing the entropy of the approximation [10]. The  
40 LME approximation may be regarded as a regularization, or (in analogy to

statistical mechanics) *thermalization*, of Delaunay triangulation which effectively resolves the degenerate cases resulting from the lack or uniqueness of the triangulation. LME basis functions possess many desirable properties for meshfree algorithms. First of all, they are entirely defined by the 45 nodal set and the domain of analysis. They are also non-negative, satisfy the partition of unity property, and provide an exact approximation of affine functions [10]. Important contributions on the Maximum-Entropy have been made by Sukumar and coworkers [11] with Cell-based techniques and the ones carried within the Optimal Transportation Meshfree (OTM) method.

50 The latter methodology has been proven to have a good performance under the dynamic regime being worth mentioning the contributions of Li *et al.* (2012) [12] and Navas *et al.* (2018) [13, 14] in the explicit regime and Navas *et al.* [15, 16, 17] and Wriggers and coworkers [18] with implicit schemes. More recently, under MPM framework, the work made by Wobbes *et al.* (2020) [19].

55 The proposed research delves into the benefits of the regularization parameter,  $\beta$ , and the analogy of the different shape functions derived by the tuning of this parameter and the traditional MPM ones.

The aforementioned techniques are devoted to mitigate the “grid crossing” error. Nevertheless, in the presence of shock waves, spurious numerical noises might appear despite of the employment of these techniques [20]. These numerical inaccuracies, also known as wiggles, arise due to inaccuracies in the time discretisation technique. A simple approach to face those spurious noises lies on the addition of nonphysical damping sources to the equilibrium equations. This approach has been widely employed in this and many other 65 numerical techniques. To avoid introducing this nonphysical sources, many researchers have proposed alternative time integration schemes which reduce the presence of high frequency noises by filtering them or increasing somehow the accuracy. One of the first attempts was the proposal of an implicit time integration scheme by Guilkey & Weiss [21]. More recently Wang *et al.* [22] mitigated these spurious noises by adding a non-viscous damping 70 to the linear momentum balance equation, and later Charlton *et al.* [23] extended this scheme to the GIMP approach introducing the Implicit GIMP (iGIMP) method. However, the local damping introduced by [22] can totally over-damp the solution in time-dependent simulations such as in consolidation process. In a recent publication, Kularathna & Soga [24] studied an 75 implicit treatment of the pressure in MPM algorithm to simulate material incompressibility avoiding artificial pressure oscillations by applying Chorin's projection. Within the explicit time integration schemes, Lu *et al.* [25] introduced the time-discontinuous Galerkin method to control the spurious noises 80 propagation, and later Tran & Solowski [20] proposed a generalised- $\alpha$  scheme for MPM with promising results but at the expense of increasing the com-

putational effort. In this paper a less time consuming and high efficient explicit predictor-corrector integration method is proposed. It consists of an accommodation of the traditional Newmark Predictor-Corrector (NPC) scheme, widely employed in Finite Element methods. This method has already been chosen in [14] among other suitable alternatives as those proposed by Wilson *et al.* (1972) [26] or Chung & Hulbert (1993) [27] because its simplicity and good performance dealing with solid dynamic problems under a meshfree framework. Other well known source of energy dissipation and numerical noise is the presence of a non-trivial null space of the linear operator that maps particles values onto nodal values. It was earlier identified by Brackbill (1984) [28] as ringing instability in the Particle in Cell (PIC) method. A recent development in the field of particle methods is a null-space filter engineered by Gritton & Berzins (2017) [29] which overcome this limitation but still introduce unwelcome damping. Later, Hammerquist & Nairn (2017) [30] introduced the XPIC as a parametric extension of the aforementioned research with excellent results.

The aim of this document is to mitigate the spurious oscillations due to inaccuracies in both space and time discretisation by the employment of a suitable combination of the LME family shape functions, and the proposal of a predictor-corrector scheme. The advantages of this approach will be illustrated through several demanding test cases on the elastic regime: the propagation of shock waves in an elastic bar and the response of a block of soil gradually loaded with gravitational forces.

The article is organised as follows : Section 2 is devoted to describe the meshfree methodology adopted in this research, first MPM procedure is introduced in 2.1, second the predictor-corrector time integration scheme is presented in 2.2, and third LME approximation scheme will be introduced in 2.3. In Section 3, applications to prove the numerical accuracy of the proposed approach are presented. Finally, conclusions and future research topics are exposed in Section 4.

## 2. The meshfree methodology

The aim of this section is to provide an overview of the standard explicit MPM algorithm [1]. Without loosing generality, the method consists of three main steps: (i) a variational recovery process, where particle data is projected onto the grid nodes, (ii) an Eulerian step, where balance of momentum equation is expressed as a nodal equilibrium equation through a FEM-like procedure, and finally (iii) a Lagrangian advection of the particles. In consequence, MPM can be regarded as a Lagrangian-Eulerian method where particles carry on all the physical information and a set of background nodes

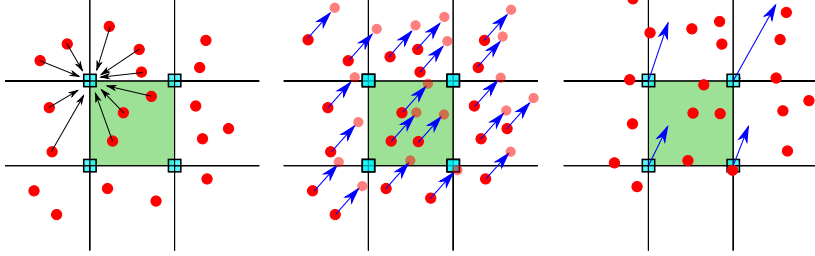


Figure 1: Description of the three steps in MPM standard algorithm.

is employed to compute the equilibrium equation. The described methodology is sketched by the scheme of the figure 1. In what follows, we will adopt the following convention: Any vector field is defined with an overarrow as  $\vec{\square}$ . Three kind of subscripts or superscripts are considered: subscript  $\square_p$  is used to define a particle variable, subscript  $\square_I$  is reserved for nodal variables, superscript  $\square^\psi$  involves a virtual magnitude. The convention adopted for the operators is as follows:  $\vec{\square}$  and  $\ddot{\square}$  are considered for the first and second time derivative,  $\square \otimes \square$  means the dyadic operator,  $\square \cdot \square$  and  $\square : \square$  are the single and double contraction of tensor index,  $\text{div}(\square)$  denotes the divergence operator, and finally  $\text{grad}(\square)$  and  $\text{grad}^s(\square)$  denotes the gradient and its symmetric part. Following, the MPM methodology, the explicit predictor-corrector scheme and LME approximation shape functions are described in subsection 2.1, 2.2 and 2.3 respectively.

### 2.1. Derivation of MPM procedure

In MPM the continuum mechanics approach is considered. We consider a region  $\Omega$  occupied by an elastic body like the sketched in the figure 2, and  $\partial\Omega$  the boundaries of the domain defined by  $\partial\Omega = \Gamma_d \cup \Gamma_n$  where  $\Gamma_d \cap \Gamma_n = \emptyset$ . In this context the field  $\vec{u}$  allows to describe the *global state* of the system. Now the variable  $\phi = (\varepsilon, \sigma)$  is defined as the set of *local states* at any point of the continuum which can be derived from the field  $\vec{u}$  through the following set of governing equations and restrictions that must be satisfied. First (i) we relate global to local state by the *compatibility equation* where the strain field  $\varepsilon$  is defined by:

$$\varepsilon = \text{grad}^s(\vec{u}), \quad (1)$$

together with essential or Dirichlet boundary conditions (DBC) at  $\Gamma_d$ . We will further assume that strains are infinitesimal. The stress field  $\sigma$  is considered the corresponding conjugate variable for the strain field, being the one which satisfies (ii) the *conservation of linear momentum equation*:

$$\rho \frac{D\vec{v}}{Dt} = \text{div}(\sigma) + \rho \vec{b} \quad (2)$$

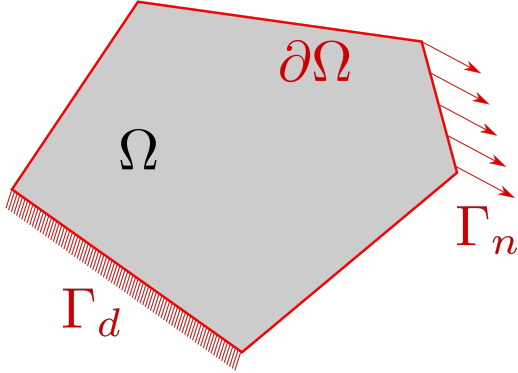


Figure 2: Description of the boundary-value-problem in a continuum. Red lines represents the closure  $\partial\Omega$  of the domain  $\Omega$  represented in gray.

together with the natural of Neumann boundary conditions (NBC) at  $\Gamma_n$ . An additional component is (iii) the constitutive equation which relates stress and strain increments as,

$$\Delta\sigma = \mathbf{D} : \Delta\varepsilon. \quad (3)$$

In this research, plane strain linear elasticity is considered. The final equation of the set is (iv) the mass conservation, which can be expressed by

$$\dot{\rho} + \rho \operatorname{div}(\vec{v}) = 0. \quad (4)$$

In order to obtain the variational statement of the problem, let us define a virtual displacement field such that

$$\vec{u}^\psi \in \mathcal{H}_0^1(\Omega) = \{\vec{u}^\psi \in \mathcal{H}^1 \mid \vec{u}^\psi = \vec{0} \text{ on } \Gamma_d\}; \quad (5)$$

where  $\vec{u}^\psi \in \mathcal{H}^1$  means that

$$\int_{\Omega} \vec{u}^\psi \cdot d\Omega < \infty \quad \text{and} \quad \int_{\Omega} \varepsilon^\psi \cdot d\Omega < \infty. \quad (6)$$

The principle of virtual work states that the equilibrium solution to the boundary-value problem of elasticity is the function  $\vec{u} \in \mathcal{H}_0^1$  such that, for any  $\vec{u}^\psi \in \mathcal{H}_0^1$ , the following holds:

$$\int_{\Omega} \rho \left( \frac{d\vec{v}}{dt} - \vec{b} \right) \cdot \vec{u}^\psi \cdot d\Omega = \int_{\Gamma_d} \vec{t} \cdot \vec{u}^\psi \cdot d\Gamma - \int_{\Omega} \sigma : \varepsilon^\psi \cdot d\Omega. \quad (7)$$

<sup>135</sup> Thus, equation (7), together with (3) and (4), represents the weak form formulation of the problem. Next, we will discretise the set of equations of the mathematical model using a double discretisation procedure, see figure 3.

First, the velocity field and the virtual displacements fields are discretised in a finite set of nodes  $\mathbf{X} = \{\vec{x}_I, I \in \mathcal{B}\} \subset \mathbb{R}^2$ , where  $\mathcal{B} = 1, \dots, n_I$ . An approximation of the continuum field can be obtained with the help of nodal values and an appropriate interpolation functions  $N_I(\vec{x})$ . Also spatial derivatives of those quantities, such as gradients and divergences, are computed through the support of the background set of nodes as

$$\varphi(\vec{x}) = \sum_{I \in \mathcal{B}} N_I(\vec{x}) \varphi_I \quad (8)$$

$$grad(\varphi)(\vec{x}) = \sum_{I \in \mathcal{B}} \varphi_I \otimes grad(N_I(\vec{x})) \quad (9)$$

Secondly, the continuum  $\Omega$  is discretised with a finite set of material points (also known as particles in this manuscript)  $\hat{\Omega} = \{\vec{x}_p, p \in \mathcal{C}\} \subset \Omega$ , where  $\mathcal{C} = 1, \dots, n_p$ . Any particle field such as position, velocity, mass, volume and stress denoted by  $\vec{x}_p$ ,  $\vec{v}_p$ ,  $m_p$ ,  $V_p$  and  $\sigma_p$ , respectively, are assigned to each material point. Furthermore, any particle field  $\varphi_p$  can be approximated within the nodes in the neighbourhood of each particle,  $\mathcal{B}_p \subset \mathcal{B}$ , and evaluating the interpolation function in the position of each particle as

$$\varphi_p = \sum_{I \in \mathcal{B}_p} N_I(\vec{x}_p) \varphi_I \quad (10)$$

$$grad(\varphi_p) = \sum_{I \in \mathcal{B}_p} \varphi_I \otimes grad(N_I(\vec{x}_p)) \quad (11)$$

The integrals appearing in the weak form (7) are evaluated by means of the Riemann integral [31] applied to a finite set of points with associated volumes  $V_p$  interpreted as quadrature weights.

$$\int_{\Omega} \varphi d\Omega = \sum_{p \in \mathcal{C}} \varphi_p V_p \quad (12)$$

Let us illustrate the procedure described above by fully developing the term of the acceleration forces in (7). Employing the definition (8), the velocity and virtual displacement fields can be approximated within its nodal values. Hence, the acceleration forces is reduced to

$$\sum_{I,J \in \mathcal{B}} \int_{\Omega} \rho N_J(\vec{x}) \frac{d\vec{v}_J}{dt} \cdot N_I(\vec{x}) \vec{u}_I^\psi d\Omega. \quad (13)$$

Rearranging terms in 13 and keeping in mind that  $\vec{u}_I^\psi$  and  $\vec{v}_J$  are nodal evaluations of  $\vec{u}^\psi$  and  $\vec{v}$ , respectively, the following expression is obtained

$$\sum_{I,J \in \mathcal{B}} \vec{u}_I^\psi \cdot \int_{\Omega} N_I(\vec{x}) \rho N_J(\vec{x}) d\Omega \frac{d\vec{v}_J}{dt}. \quad (14)$$

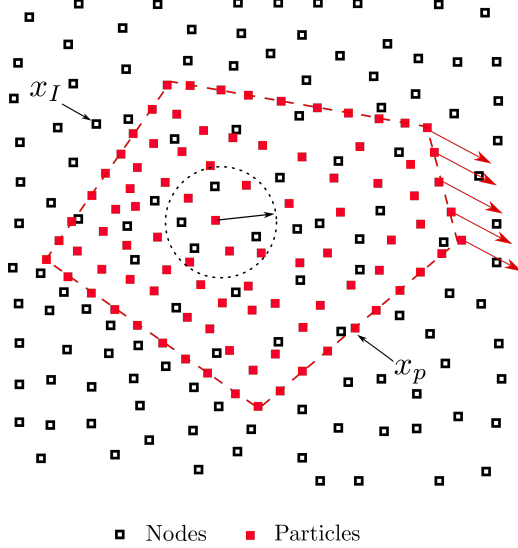


Figure 3: Description of the spatial discretisation for domain presented in the figure 2. Blue mesh represents the background computational support, and the red mesh conforms the discretised continuum body.

and by means of (12), and keeping in mind that expression (14) is for any  $\vec{u}^\psi \in \mathcal{H}_0^1$ , the following discrete expression of the acceleration can be derived

$$\begin{aligned}
& \sum_{I,J \in \mathcal{B}} \sum_{p \in \mathcal{C}} N_{Ip} \rho_p N_{Jp} V_p \frac{d\vec{v}_J}{dt} = \\
&= \sum_{I,J \in \mathcal{B}} \sum_{p \in \mathcal{C}} N_{Ip} m_p N_{Jp} \frac{d\vec{v}_J}{dt} = \\
&= \mathbf{m}_{IJ} \frac{d\vec{v}_J}{dt}
\end{aligned} \tag{15}$$

Where  $\mathbf{m}_{IJ}$  is the nodal mass matrix, and  $N_{Ip}, N_{Jp}$  are the interpolation functions for nodes  $I, J$  evaluated at the position of each particle  $p$ . In order to improve computational efficiency and stability, the nodal mass matrix can be substituted by the lumped mass matrix  $\mathbf{m}_{IJ}^{lumped}$ . The remaining terms of (7) are obtained within a similar procedure and can be found in literature, see for instance [32]. Therefore equation (7) can be discretised as

$$\mathbf{m}_{IJ} \frac{d\vec{v}_J}{dt} = \sum_{p \in \mathcal{C}} -\underbrace{\sigma_p \cdot \text{grad}(N_{Ip}) V_p}_{f_I^{int}} + \underbrace{N_{Ip} \vec{b}_p m_p + N_{Ip} \vec{t}_p V_p h^{-1}}_{f_I^{ext}} \tag{16}$$

Where  $h$  is the solid thickness in 2D and  $\sigma_p = \sigma_p(\varepsilon_p)$  is the stress field at particle  $p$ , which can be obtained after considering a suitable constitutive

model. The particle strain field is approximated thorough the time integration of the rate of strain tensor, that is computed employing the velocity at the background set of nodes by means of the equation

$$\dot{\varepsilon}_p = \frac{\Delta\varepsilon_p}{\Delta t} = \sum_{I \in \mathcal{B}_p} \frac{1}{2} [grad(N_{Ip}) \otimes \vec{v}_I + \vec{v}_I \otimes grad(N_{Ip})]. \quad (17)$$

Finally, mass conservation is guaranteed by means of (4) which can be rewritten in terms of the rate of strain tensor  $\dot{\varepsilon}$  as

$$\dot{\rho} = -\rho \operatorname{trace}(\dot{\varepsilon}). \quad (18)$$

Equation (16) is a second order ordinary differential equation in time and a time integration scheme is required. To this end, time is discretised into a finite set of time steps  $k = 1 \dots, N_t$ , where  $k$  is the current time step and  $N_t$  is the total number of time steps. Once the nodal equilibrium equation is solved, the values at the nodes are interpolated back into the particles, which are advected to the new position through:

$$\dot{\vec{v}}_p = \sum_{I \in \mathcal{B}_p} N_{Ip} \vec{a}_I, \quad \text{and} \quad \dot{\vec{x}}_p = \sum_{I \in \mathcal{B}_p} N_{Ip} \vec{v}_I. \quad (19)$$

Traditionally, Eqs. (16) and (19), are solved with an explicit forward Euler algorithm. In the following subsection, [this well known algorithm and the proposed schemes are described.](#)

## 2.2. MPM time integration scheme: the Newmark Predictor-Corrector proposal

As stated previously, an explicit forward Euler algorithm has been utilized widely within the MPM methodology. This scheme has been described in detail by many researchers [1], [33], [34]. Other authors have proposed many others time integration alternatives like [21, 23, 20]. In the first publication on MPM [1], [the nodal acceleration was considered to update the particles by](#)

$$\vec{v}_p^{k+1} = \vec{v}_p^k + \sum_{I \in \mathcal{B}_p} \Delta t N_{Ip} \vec{a}_I^k, \quad (20)$$

$$\vec{x}_p^{k+1} = \vec{x}_p^k + \sum_{I \in \mathcal{B}_p} \Delta t N_{Ip} \vec{v}_I^k. \quad (21)$$

However, as Andersen (2009)[34] pointed out, this algorithm has been shown to be numerically unstable due to [the fact](#) that nodal forces can be infinite for an infinitesimal nodal mass  $\mathbf{m}_I$ . This issue may lead to numerical problems

when nodal acceleration is obtained in the evaluation of the Eqs. (21) and (20). Hence, a corrected version of this algorithm was proposed by Zhang *et al.* (2016)[32]:

$$\vec{x}_p^{k+1} = \vec{x}_p^k + \sum_{I \in \mathcal{B}_p} \Delta t \frac{N_{Ip} \vec{p}_I^k}{\mathbf{m}_I}, \quad (22)$$

$$\vec{v}_p^{k+1} = \vec{v}_p^k + \sum_{I \in \mathcal{B}_p} \Delta t \frac{N_{Ip} \vec{f}_I^k}{\mathbf{m}_I}. \quad (23)$$

Delving into the improvement of the accuracy of the MPM explicit schemes, Tran & Solowski (2019)[20] presented a generalized- $\alpha$  scheme for MPM inspired in the explicit time integration algorithm proposed by Chung & Hulbert (1993)[27], but with the particularity that the acceleration is evaluated both **at** the beginning and **at** the end of the time step.

$$\vec{v}_p^{k+1} = \vec{v}_p^k + \sum_{I \in \mathcal{B}_p} \Delta t N_{Ip} [(1 - \gamma) \vec{a}_I^k + \gamma \vec{a}_I^{k+1}], \quad (24)$$

$$\vec{x}_p^{k+1} = \vec{x}_p^k + \sum_{I \in \mathcal{B}_p} N_{Ip} \left[ \Delta t \vec{v}_I^k + \Delta t^2 \left( \left( \frac{1}{2} - \beta \right) \vec{a}_I^k + \beta \vec{a}_I^{k+1} \right) \right], \quad (25)$$

$$\vec{a}_p^{k+1} = \sum_{I \in \mathcal{B}_p} N_{Ip} \vec{a}_I^{k+1}. \quad (26)$$

This scheme has been proven to damp out the highest frequency noises [20]. However, it can present the same numerical instabilities as in (21),(20) when nodal masses become infinitesimal, and requires extra storage for nodal values of acceleration and previous steps.

In this section, an explicit predictor-corrector time integration scheme is proposed, which is based on the Newmark central differences explicit scheme. This method is devoted to solve system of equations of the type

$$\sum_{J \in \mathcal{B}} \mathbf{M}_{IJ} \ddot{\mathbf{d}}_J + \mathbf{C}_{IJ} \dot{\mathbf{d}}_J + \mathbf{K}_{IJ} \mathbf{d}_J = \mathbf{F}_I.$$

The presence of a background grid of nodes allows to apply this integration method within the MPM framework in a similar manner that the one proposed by Tran *et al.* [20]. By using the predictor step it is possible to calculate nodal velocities and update particles position employing nodal values of velocity and acceleration.

The predictor-corrector algorithm has been described in the classic literature [35], and its stability and computational advantages were widely validated by Liu [36]. The “classic” Newmark Predictor-Corrector (NPC) algorithm starts with a predicted value of the nodal velocities at the  $(k + 1)$ th time step, denoted by  $\bar{v}_I^{pred}$ , which is calculated as follows:

$$\bar{v}_I^{pred} = \bar{v}_I^k + (1 - \gamma) \Delta t \bar{a}_I^k. \quad (27)$$

The *user-defined* parameter  $\gamma \geq 0$  that appears in (27), influences both the predictor accuracy and the stability of the algorithm. As pointed out Liu [36], the truncation error of the predictor formula is  $O(\Delta t^3)$  when  $\gamma = 0.5$ , and is unconditionally stable if  $0 < \gamma \leq 0.25$ . To accommodate this step to MPM framework, it is necessary to get the nodal values of the velocity and acceleration throughout a variational recovery process where particles quantities are transferred to the mesh nodes. This technique arises as a generalization of the super-convergent recovery procedures described by Zienkiewicz & Zhu [37] (*ZZ*) in the context of FEM. Bardenhagen & Kober [3] proved that through this information-transference technique mass and momentum are conserved. For a general particle variable  $\Phi_p$  it is possible to get its nodal homologous  $\Phi_I$  by means of the *ZZ* technique as:

$$\Phi_I = \sum_{p \in C} \frac{m_p N_{Ip} \Phi_p}{m_I}. \quad (28)$$

Therefore, to get an analogous expression for (27) in the context of MPM, the procedure described in the equation (28) is employed, obtaining the following expression:

$$\bar{v}_I^{pred} = \sum_{p \in C} \underbrace{\frac{N_{Ip} m_p \bar{v}_p^k}{m_I}}_{\bar{v}_I^k} + (1 - \gamma) \Delta t \underbrace{\frac{N_{Ip} m_p \bar{a}_p^k}{m_I}}_{\bar{a}_I^k}. \quad (29)$$

However, this way of computing the predictor stage can introduce instabilities due to numerical cancellation likewise the original Sulky algorithm. This issue can be avoided easily by the equivalent formulation inspired in the *ZZ* technique,

$$\bar{v}_I^{pred} = \sum_{p \in C} \frac{N_{Ip} m_p (\bar{v}_p^k + (1 - \gamma) \Delta t \bar{a}_p^k)}{m_I}. \quad (30)$$

This way of computing the nodal predictor is numerically stable and minimize the computational effort. Once nodal velocities are obtained, the DBC

are imposed over  $\Gamma_d$ . Next the *corrector* step is introduced. Predicted nodal velocities obtained in (30), are now corrected by the equation

$$\vec{v}_I^{k+1} = \vec{v}_I^{pred} + \gamma \Delta t \frac{\vec{f}_I^k}{\mathbf{m}_I}. \quad (31)$$

Finally particle accelerations, velocities and positions are updated as,

$$\vec{a}_p^{k+1} = \sum_{I \in \mathcal{B}_p} \frac{N_{Ip} \vec{f}_I^k}{\mathbf{m}_I} \quad (32)$$

$$\vec{v}_p^{k+1} = \vec{v}_p^n + \sum_{I \in \mathcal{B}_p} \Delta t \frac{N_{Ip} \vec{f}_I^k}{\mathbf{m}_I} \quad (33)$$

$$\vec{x}_p^{k+1} = \vec{x}_p^n + \sum_{I \in \mathcal{B}_p} \Delta t N_{Ip} \vec{v}_I^k + \frac{1}{2} \Delta t^2 \frac{N_{Ip} \vec{f}_I^k}{\mathbf{m}_I}. \quad (34)$$

In the proposed scheme, accelerations (32) and velocities (33) are computed with information coming from the predictor step. On the other hand, positions (34) are evaluated with information coming from the corrector step in the velocity term, while acceleration term introduces information from the corrector. Therefore, it can be appreciated some similarities with the *leapfrog scheme* [32], where position is not updated at full time step, but the velocity is updated at half time steps. Notice also that, with this approach, the calculation of nodal momentum values are not required. Due to its simplicity, the proposed scheme can be implemented with minor modifications over the standard forward Euler. The full implementation is summarized in the algorithm 1.

### 2.3. Local Max-Ent approximants

The popularity of the MPM has increased notoriously during the recent years due to its ability to deal with large strain problems without mesh distortion issues inherent to mesh based methods like FEM, see Więckowski [38]. However, in the simulations made with the original MPM, numerical noises appear when particles cross the cell boundaries. Solving this issue is the main goal of the employment of the LME shape functions. Local Maximum-Entropy (LME) approximation schemes were first introduced by Arroyo & Ortiz (2006)[10] and has been recently tested under MPM framework by Wobbes *et al.* (2020)[19]. The simulations presented in [19] of MPM within LME show considerably more accurate stress approximations than traditional MPM schemes. However, how the regularization parameter  $\beta$  affects to the accuracy and stability of the solution is not assessed deeply in

---

**Algorithm 1** Newmark Predictor-Corrector (NPC) scheme

---

- 1: **Update mass matrix.**
- 2: **Explicit Newmark Predictor.**

$$\vec{v}_I^{pred} = \sum_{p \in \mathcal{C}} \frac{N_{Ip}^k m_p (\vec{v}_p^k + (1 - \gamma) \Delta t \vec{a}_p^k)}{m_I}.$$

- 3: **Impose essential boundary conditions.**

At the fixed boundary, set  $\vec{v}_I^{pred} = 0$ .

- 4: **Deformation tensor increment calculation.**

$$\dot{\varepsilon}_p^{k+1} = \sum_{I \in \mathcal{B}_p} \left[ \vec{v}_I^{pred} \otimes \text{grad}(N_{Ip}^{k+1}) \right]^s \quad \text{and} \quad \Delta \varepsilon_p^{k+1} = \Delta t \dot{\varepsilon}_p^{k+1}.$$

- 5: **Update the density field.**

$$\rho_p^{k+1} = \frac{\rho_p^k}{1 + \text{trace} [\Delta \varepsilon_p^{k+1}]}.$$

- 6: **Balance of forces calculation.**

Calculate the total grid nodal forces by evaluating the right hand side of (16) with the information from the predictor step. In those nodes where  $\frac{\partial \vec{v}_I^k}{\partial t} \Big|_{\Gamma_d} = 0$ , the acceleration is fixed to zero and nodal forces are stored as reactions.

- 7: **Explicit Newmark Corrector.**

$$\vec{v}_I^{k+1} = \vec{v}_I^{pred} + \gamma \Delta t \frac{\vec{f}_I^{k+1}}{\mathbf{m}_I^{k+1}}.$$

- 8: **Update particles lagrangian quantities.**

$$\begin{aligned} \vec{a}_p^{k+1} &= \sum_{I \in \mathcal{B}_p} \frac{N_{Ip}^k \vec{f}_I^k}{\mathbf{m}_I^k}, \\ \vec{v}_p^{k+1} &= \vec{v}_p^n + \sum_{I \in \mathcal{B}_p} \Delta t \frac{N_{Ip}^k \vec{f}_I^k}{\mathbf{m}_I^k}, \\ \vec{x}_p^{k+1} &= \vec{x}_p^n + \sum_{I \in \mathcal{B}_p} \Delta t N_{Ip}^k \vec{v}_I^k + \frac{1}{2} \Delta t^2 \frac{N_{Ip}^k \vec{f}_I^k}{\mathbf{m}_I^k}. \end{aligned}$$

- 9: **Reset nodal values.**
-

that research. The tuning of this  $\beta$  parameter allows to make the comparison of the accuracy against analogous traditional MPM shape function.

The basic idea of the shape functions based on such an estimate is to interpret the shape function  $N_I(\vec{x})$  as a probability. This allows us to introduce two important limits: the principle of maximum-entropy (*max-ent*) statistical inference stated by [39], and the Delaunay triangulation which ensures the minimal width of the shape function.

This approximation scheme represents an optimal compromise, in the sense of Pareto, between the *unbiased statistical inference* based on the nodal data which leads to the principle of *Maximum-Entropy* stated by Jaynes [39], and the definition of local shape functions of *least width* the least biased shape functions.

Following [10], entropy of a discrete random variable can be defined as the uncertainty of the random variable. A measure of this uncertainty can be obtained by means of Shannon's entropy:

$$H(p_1, \dots, p_n) = - \sum_{I=1}^{N_n} p_I \log p_I \quad (35)$$

where  $p_I$  stands for probability of the random variable outcomes. By interpreting these probabilities as the shape functions  $N_I(\vec{x})$  of an approximation scheme, equation (35) can be regarded as a measure of the uncertainty of the approximation. Thus, according to Jaynes's principle of maximum entropy [39], the least-biased approximation scheme can be given by

$$\begin{aligned} \text{(LME) Maximize } H(N_I) &\equiv - \sum_I^{N_n} N_I(\vec{x}) \log N_I \\ \text{subject to } & \begin{cases} N_I \geq 0, \quad I=1, \dots, n \\ \sum_{I=1}^{N_n} N_I = 1 \\ \sum_{I=1}^{N_n} N_I \vec{x}_I = \vec{x} \end{cases} \end{aligned}$$

On the other hand, the control of the shape function width and its decay with distance away from the corresponding nodes is a desirable property. To

reach to this objective [10] propose the following linear program,

$$(RAJ) \text{ For fixed } \vec{x} \text{ minimize } U(\vec{x}_p, N_I) \equiv \sum_I N_I |\vec{x}_p - \vec{x}_I|^2$$

subject to  $\begin{cases} N_I \geq 0, I=1, \dots, n \\ \sum_{I=1}^{N_n} N_I = 1 \\ \sum_{I=1}^{N_n} N_I \vec{x}_I = \vec{x} \end{cases}$

To reach a compromise between the two competing objectives, a Pareto set is considered [10]

$$(LME)_\beta \text{ For fixed } \vec{x} \text{ minimize } f_\beta(\vec{x}, N_I) \equiv \beta U(\vec{x}, N_I) - H(N_I)$$

subject to  $\begin{cases} N_I \geq 0, I=1, \dots, n \\ \sum_{I=1}^{N_n} N_I = 1 \\ \sum_{I=1}^{N_n} N_I \vec{x}_I = \vec{x} \end{cases}$

The regularization or *thermalization* parameter between the two criterion,  $\beta$ , has Pareto optimal values in the range  $\beta \in (0, \infty)$ . The unique solution of the local *max-ent* problem  $LME_\beta$  is:

$$N_I^*(\vec{x}) = \frac{\exp \left[ -\beta |\vec{x} - \vec{x}_I|^2 + \vec{\lambda}^* \cdot (\vec{x} - \vec{x}_I) \right]}{Z(\vec{x}, \vec{\lambda}^*)} \quad (36)$$

where

$$Z(\vec{x}, \vec{\lambda}) = \sum_{I=1}^{N_n} \exp \left[ -\beta |\vec{x} - \vec{x}_I|^2 + \vec{\lambda} \cdot (\vec{x} - \vec{x}_I) \right] \quad (37)$$

being  $\vec{\lambda}^*(\vec{x})$  the unique minimiser for the function  $\log Z(\vec{x}, \vec{\lambda})$ . The traditional way to obtain such a minimiser is using Eq. (38) to calculate small increments of  $\partial \vec{\lambda}$  in a Newton-Raphson approach.  $\mathbf{J}$  is defined as the Hessian matrix, obtained by:

$$\mathbf{J}(\vec{x}, \vec{\lambda}, \beta) \equiv \frac{\partial \vec{r}}{\partial \vec{\lambda}} \quad (38)$$

$$\vec{r}(\vec{x}, \vec{\lambda}, \beta) \equiv \frac{\partial \log Z(\vec{x}, \vec{\lambda})}{\partial \vec{\lambda}} = \sum_I^{N_n} p_I(\vec{x}, \vec{\lambda}, \beta) (\vec{x} - \vec{x}_I) \quad (39)$$

In order to obtain the first derivatives of the shape function, it is also necessary to compute  $\nabla N_I^*$

$$\nabla N_I^* = N_I^* \left( \nabla f_I^* - \sum_J^{N_n} N_J^* \nabla f_J^* \right) \quad (40)$$

where

$$f_I^*(\vec{x}, \vec{\lambda}, \beta) = -\beta |\vec{x} - \vec{x}_I|^2 + \vec{\lambda}(\vec{x} - \vec{x}_I) \quad (41)$$

Employing the chain rule, rearranging and considering  $\beta$  as a constant, Arroyo and Ortiz [10] obtained the following expression for the gradient of the shape function.

$$\nabla N_I^* = -N_I^* (\mathbf{J}^*)^{-1} (\vec{x} - \vec{x}_I) \quad (42)$$

The regularization parameter  $\beta$  of LME shape functions may be controlled by adjusting a dimensionless parameter<sup>2</sup>,  $\hat{\gamma} = \beta h^2$  [10], where  $h$  is defined as a measure of the nodal spacing. Since  $N_I$  is defined in the entire domain, in practice, the function  $\exp(-\beta \vec{r})$  truncated by a given tolerance,  $10^{-6}$  in this research, would ensure a reasonable range of neighbours (see [10] for details). This tolerance defines the limit values of the influence radius and is used thereafter to find the neighbour nodes of a given integration point. An additional remark is that, analogous to alternative non-polynomial meshfree basis functions, the LME approximation scheme requires more than  $d + 1$  nodes to determine the values of the shape functions as well as their derivatives at any point in the convex hull of the nodal set, where  $d$  is the dimension of the problem.

This interpolation technique avoids important shortcomings when using GIMP or B-Spline MPM regarding the computational domain boundaries (see Steffen *et al.* (2008)[40]), which are related to additional considerations in the application of the boundary conditions. Motivated by their increased extents, particles may share an influence radius that lies outside of the simulation domain. Some researchers have solved this problem with the so called “extra” or “ghost” nodes. These nodes require especial treatment, similar to those employed in the Smoothed Particle Hydrodynamics (SPH), for further details see Liu & Liu (2003)[41]. The approach here described does not require the employment of this artifices. Due to the FEM-compatibility,

---

<sup>2</sup>To avoid confusion with the  $\gamma$  parameter of the NPC, the dimensionless parameter defined by Arroyo & Ortiz [10] as  $\gamma$  will be represent by  $\hat{\gamma}$  to preserve as much as possible the original notation.

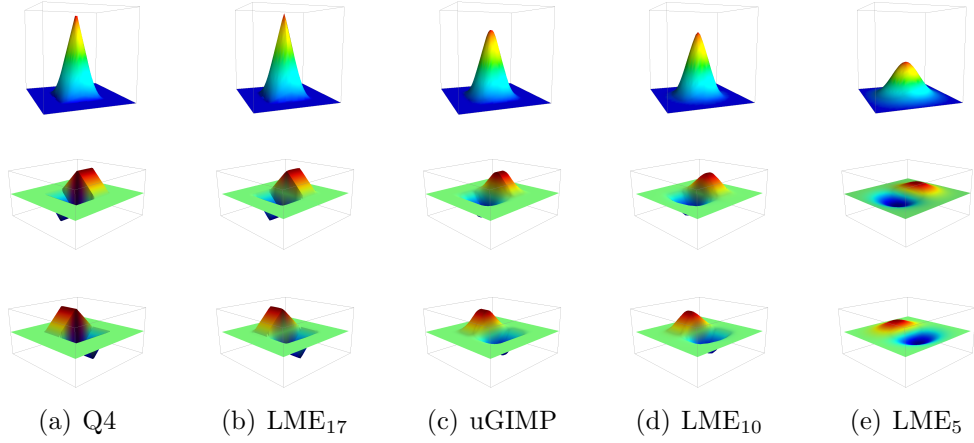


Figure 4: Comparative of linear piecewise shape functions (Q4) and uGIMP shape functions *versus* LME approximation for a two-dimensional arrangement of nodes, and spatial derivatives for several values of  $\hat{\gamma} = \beta h^2$ .

the LME shape function is degenerated to linear finite element shape function if  $d + 1$  neighbouring nodes are chosen as the support, where  $d$  is the  
220 number of dimensions in the problem. Figure 4 shows that larger values  
of the parameter  $\beta$  make the solution to tend to the linear FEM solution  
as the athermal limit is reached [10]. Ullah *et al.* [42] took advantage of  
the LME FEM-compatibility to couple the Element-Free Galerkin Method  
(EFGM) and FEM for linear elasticity and for problems with both material  
225 and geometrical non-linearities. Furthermore, with a conveniently adopted  
regularization parameter it is possible to get a GIMP-like shape function.  
Finally SPH-like behaviour can be obtained for lower values of  $\hat{\gamma}$  since the  
support of the shape function is drastically increased, and therefore *smoother*  
solutions are obtained. See [15] for an application of this capability, where  
230 oscillations due to excess of pore water pressure in consolidation problems  
are smoothed out by using this technique. The employment of smoothing  
algorithms is also straightforward in the fluid-solid interaction problems [43].  
This behaviour was noticed previously by [10], were authors highlighted how,  
235 by adjusting the spatial variation of  $\beta(\vec{x})$ , it is possible to select regions of  
the domain of analysis which are treated by finite elements and regions that  
are treated in the style of meshfree methods, with seamless transitions  
between those regions. The aforementioned adaptability can be appreciated in  
figure 4.

In this research and in [10],  $\beta$  is a scalar as the influence area of the shape  
240 function is controlled by the Euclidean norm, therefore the search area is  
geometrically a circle in 2D, or a sphere in 3D. Building upon the idea of

anisotropic shape functions, [44] introduced an enhanced version of the original LME scheme, which uses an anisotropic support to deal with tensile instability. This is another benefit of the proposed methodology, that, although is out of the scope of the present document, will be incorporated in future research.

Unfortunately, the employment of *max-ent* approximants is not free of pitfalls. Some requirements such as the need for a convex domain, as well as those derived from its calculation (the determination of the Lagrange Multipliers, specially at the boundaries, or the obtainment of the minimizer of the logarithmic function), make the usage of it a challenging tool. Concerning the convex domain requirement, Arroyo & Ortiz [10] briefly discussed the existence of non-convex domains, and proposed some solutions to it. For instance, the possibility of replacing the Euclidean distance  $\|x - x_a\|$  in the definition of the shape functions by the length of the shortest path contained within the domain connecting  $x$  and  $x_a$ ; or by decomposing the non-convex domain into convex sub-domains. Of course the requirement of convex domain is not exclusive from *max-ent*, it also concerns to the remaining interpolation techniques in the MPM and other meshfree methods. For instance, this topic has been extensively studied in the context of MLS-based meshfree methods, for instance visibility, diffraction, and constrained path criteria. These methods are directly applicable to local *max-ent* approximation.

Despite these drawbacks, the results depicted in this manuscript will strengthen the motivation of its employment in order to mitigate typical MPM problems such as cell-crossing or stress instabilities in a wide range of problems.

### 3. Application to linear elasticity dynamic problems.

This section is devoted to test the ability of both predictor-corrector time integration scheme and the Local *Max-Ent* approximants to overcome spurious oscillations due to the grid crossing and high frequency loads under the context of MPM. Three different tests have been adopted for this purpose: The first example is the well known benchmark proposed by Dyka & Ingel (1995)[46]. It is devoted to test the accuracy of the Newmark Predictor-Corrector (NPC) scheme. The second example is the test proposed in the PhD thesis of Andersen (2009)[34] where the evolution of velocity waves in an elastic square. In the third example the present approach is tested under a scenario where shocks and grid crossing occurs. All simulations were performed with in-house software.

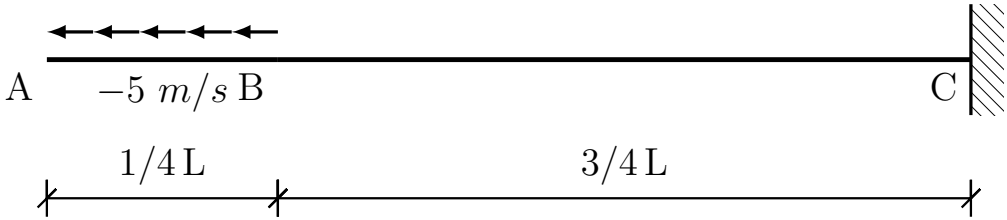


Figure 5: Geometrical description of the Dyka [46] bar.

280 3.1. *Dyka's bar* [46]

This benchmark was proposed by Dyka [46] since allows to study easily the capability of the proposed time integration algorithm to avoid velocity field instabilities. It consists of a one-dimensional bar of a length of 0.1333 meters, sketched in the figure 5. The boundary conditions are: displacements are constrained ( $\vec{v}|_{x=L} = 0$ ) in the right border, being free on all other boundaries. An initial velocity of  $\vec{v}_o = -5 \text{ m/s}$  is given to the left quarter of the bar. Finally, the elastic parameters chosen for this test are:

- Density :  $7833 \text{ kg/m}^3$
- Poisson ratio : 0
- Elastic modulus :  $200 \cdot 10^9 \text{ Pa}$

290 In the proposed example, the simulation extends from time zero up to  $10^{-4}$  s. This time interval allows the elastic wave to travel a distance of 2.6 lengths of the bar. For the spatial discretisation, a set of seven nodal mesh sizes (0.1, 0.3325, 0.5, 1.0, 3.3325, 6.665, 10.0 millimeters) are considered. For each element a number of four particles was selected. In the initial layout, particles are located the exact quadrature points of a linear quadrilateral, with the exception of the uGIMP simulation, where gaps or overlap between voxels of each particle are not allowed. In those cases, each particle occupies the center of each cell quarter. For all simulations, time step is controlled by a Courant-Friedrichs-Levy condition of 0.1, were the adopted celerity is computed as:

$$Cel = \max\left\{\max_{p \in \Omega_p}\{\vec{v}_p\}, \max_{p \in \Omega_p}\left\{\sqrt{\frac{E_p}{\rho_p}}\right\}\right\}. \quad (43)$$

An important consideration regarding modellization concerns the background mesh. Notice that free border of the bar has a maximum horizontal displacement of 0.03 millimeters, therefore a computational domain with an extra gap

of 0.03 millimeters is required in order to accommodate the unconstrained  
 295 displacement of the particles in the left border of the bar. This problem arises  
 when the mesh size is small enough that relative displacement of the particles  
 is larger **than** the distance to the border, so grid crossing phenomena could  
 appear even in those cases with infinitesimal displacements. In this case, an  
 300 analytical solution can be obtained through the characteristics method, de-  
 scribed in the appendix Appendix A. This section contains a large number  
 of comparisons, which have been summarised in Table 1. First, a conver-  
 gence study regarding the integration scheme and interpolation technique is  
 performed in 3.1.1. Second, comparison of the capabilities of the NPC and  
 305 FE algorithms to damp out numerical noise is analysed in 3.1.2. Third, the  
 response of the LME approximation for different  $\hat{\gamma}$  values is study in 3.1.3.  
 Fourth, comparison between the well-known uGIMP shape function against  
 the LME approximation is performed in 3.1.4. Finally, a comparison between  
 the MPM and the Optimal Transportation Meshfree (OTM) method, using  
 310 the same time integration scheme and interpolation technique, is conducted  
 in 3.1.5.

### 3.1.1. Convergence analysis

To measure the convergence of the solutions for the different time inte-  
 gration and approximation schemes the root-mean-square (RMS) error in the  
 velocity field is computed. RMS error is defined as

$$RMS = \sqrt{\frac{1}{N} \sum_p^N (\vec{v}_p - \hat{\vec{v}}_p)^2}, \quad (44)$$

where  $\vec{v}_p$  and  $\hat{\vec{v}}_p$  are respectively the analytical and numerical solutions eval-  
 uated in the final time step in the position of each particle. In Fig. 6 the  
 315 evolution of the RMS is obtained for both time integration schemes. The  
 right figure, with the NPC results, shows lower values of the estimated error,  
 denoting the higher performance of this methodology. About the spatial dis-  
 cretisation, the LME schemes show an error comparable to the obtained with  
 the uGIMP, being even lower close to the *grid-crossing region*. In this region  
 the performance is punished with significant movement of the particles as far  
 320 as the mesh size is reduced.

Figure (6) also highlights how on the one hand the slope of the LME error  
 decreases monotonously for the lower  $\hat{\gamma}$  values up to the *grid-crossing region*  
 (dark grey region), where more error is accumulated. On the other hand,  
 when higher values of  $\hat{\gamma}$  are considered in LME and also for the uGIMP  
 325 and the bi-linear shape functions, the change in error slope occurs in the

	3.1.1	3.1.2	3.1.3	3.1.4	3.1.5
MPM-Q4-FE	x	x			
MPM-uGIMP-FE	x	x			
MPM-LME <sub>2,0</sub> -FE	x	x	x	-	
MPM-LME <sub>3,0</sub> -FE	x	x	-		
MPM-LME <sub>4,0</sub> -FE	x	x	-		
OTM-LME <sub>4,0</sub> -FE				x	-

Table 1: Table with all the permutations for the Dyka bar [46].

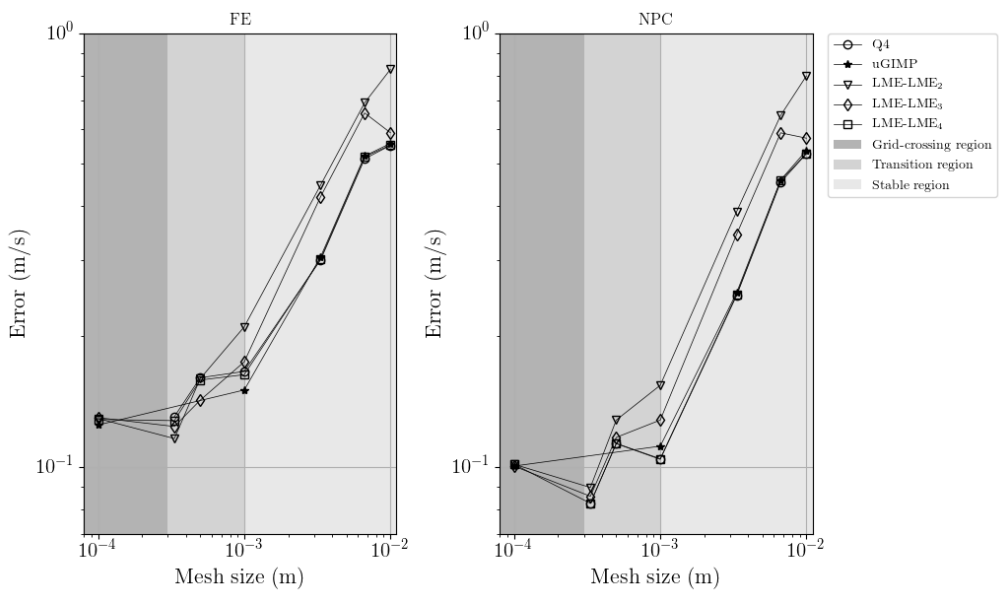


Figure 6: Velocity error evolution at the point A in the Dyka's bar , convergence plots for FE and NPC. The plot is subdivided with colours, the darker part of the diagram shows coincides when the relative movement of the particles is large enough to produce the grid crossing phenomena. The lightest part of the diagram coincides when the relative movement of the particles in negligible in comparison with the mesh size. And in the middle region a transition behaviour take place.

*transition region* (middle grey region). It might be concluded that the latter methods are more sensitive to grid crossing than the former.

Finally, the absence of uGIMP values for a mesh size of 0.3325 and 0.5 millimeters in figure (6) is remarkable. The reason is due to an unstable increasing of the error suffered during uGIMP simulations for these mesh sizes. A feasible explanation for this phenomena could be the presence of numerical cancellation which could produce gaps between voxels. Further research should be done in this direction for getting a better comprehension of this phenomenon. Conversely, this shortcoming is not suffered by LME, independently of regular or irregular nodal layout.

### 3.1.2. FE versus NPC

A first comparison of the performance of both time integration schemes is presented in figure 7. Both integration schemes show numerical oscillations with respect to the analytical solution all over the simulation time, being worse just after jump discontinuities. However, the NPC approach damps out these oscillations faster than the FE scheme. The oscillations of the NPC almost disappeared before reaching subsequent jump discontinuities, while those of FE do not. Moreover, oscillations of the FE seems to increase further after each jump discontinuity and an unstable tendency can be foreseen. This unstable tendency is not appreciated in the NPC integration scheme.

### 3.1.3. Sensitive analysis to $\hat{\gamma}$ parameter

Figure (8) shows the sensitivity of the LME approximation scheme to variations in the parameter  $\hat{\gamma}$ , which is the one that controls the value of the regularization parameter  $\beta$  together with the nodal spacing parameter  $h$ . It can be observed that for lower values of  $\hat{\gamma}$  the numerical solution presents a faster decay of the spurious oscillations. This capability could be useful in simulations where extremely noisy oscillations could damage the solutions like memory materials. An additional observation, concerning to the solution sensibility depending on the regularization parameters, is the behaviour of the solution depending on the decreasing of mesh size. For larger mesh sizes, where the relative particle displacement is negligible in comparison with the cell size, the global behaviour is FEM-like, therefore, larger values of  $\hat{\gamma}$  may offer better results. On the other hand, when mesh size is small enough to produce grid-crossing, meshfree behaviour is required to ensure the convergence of the solution and tiny values of  $\hat{\gamma}$  may lead to better performances.

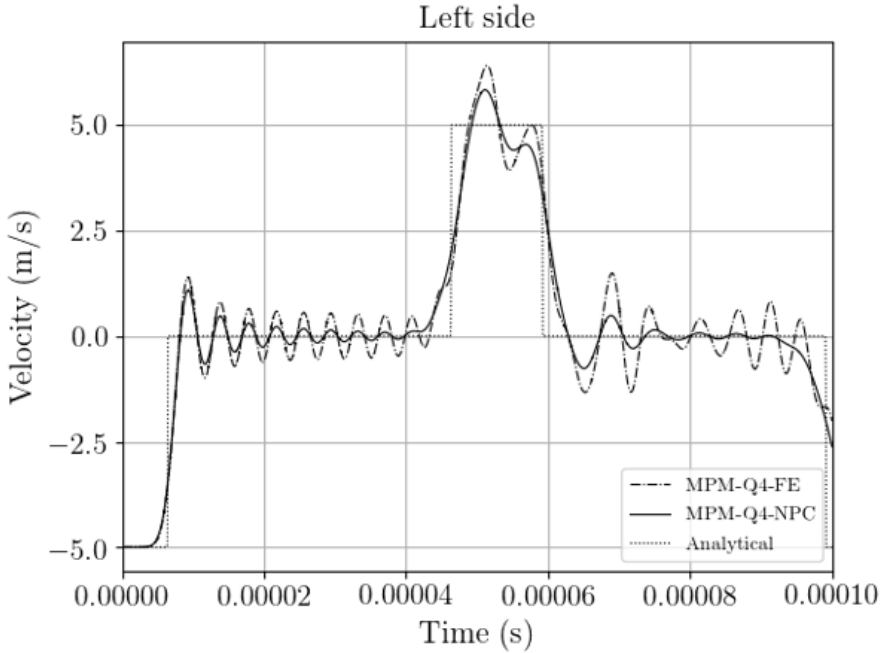


Figure 7: Comparison of NPC and FE performances: In the picture the velocity evolution at the point in the bar left side is plotted.

### 3.1.4. LME versus uGIMP

The performance of the uGIMP [3] shape function *versus* the LME approximation scheme with a dimensionless regularization parameter  $\hat{\gamma}$  of 4.0 is compared in Figure 9. Although remarkable differences are not observed under a regular mesh, LME approximants seems to fits better than uGIMP after the jump.

### 3.1.5. OTM versus MPM

Finally, the MPM approach is compared with the Optimal Transportation Meshfree (OTM) [47] method, both with the same time integration scheme, spatial discretisation and interpolation technique. Results of the comparison are shown in figure 10. During the first half of the simulation both methods seem to perform in a similar way, but during the second half of the simulation after the elastic wave has traveled from the free border to the fixed one and back, in OTM the solution becomes more noisy than the one performed by MPM.

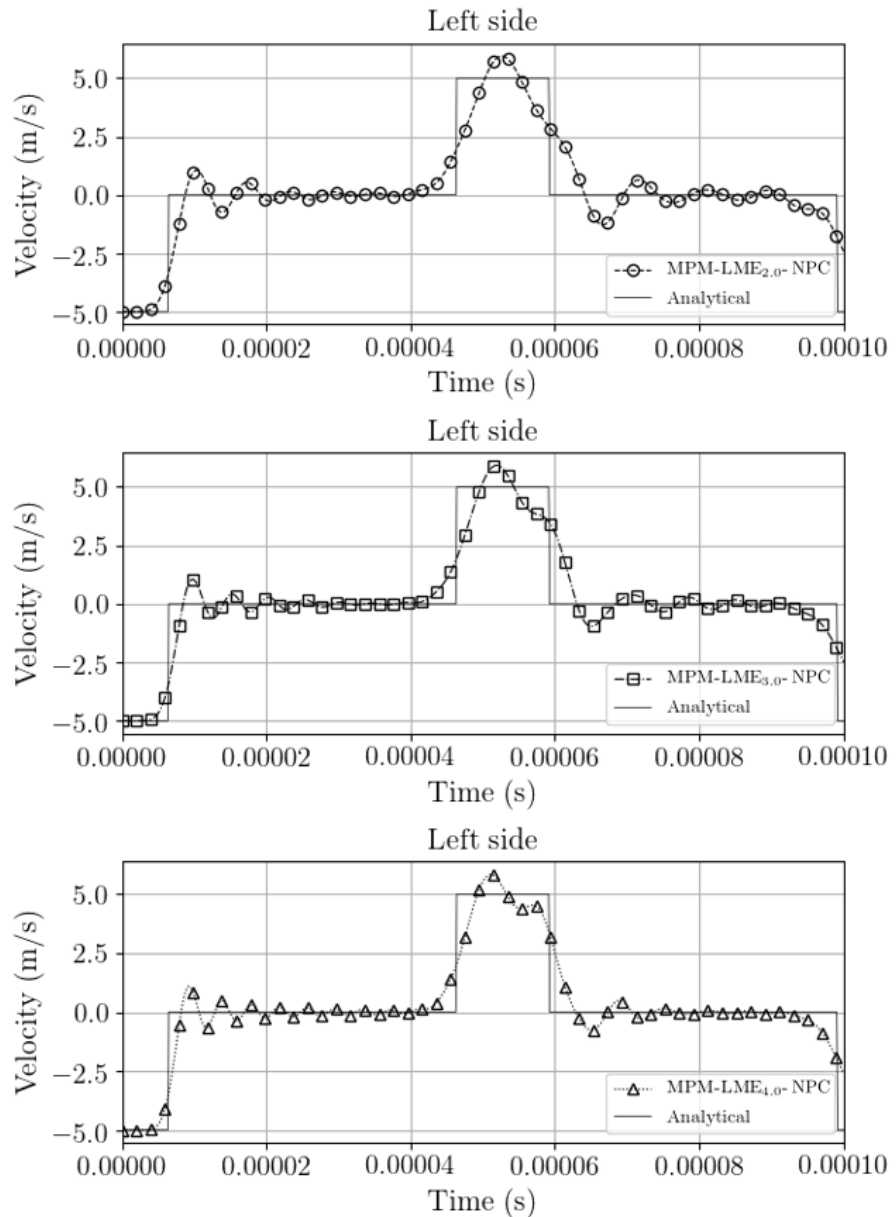


Figure 8: Sensitivity of LME approximants performance to changes in the dimensionless regularization parameter  $\hat{\gamma}$ . To illustrate it, the velocity evolution at the point in the bar left side is plotted.

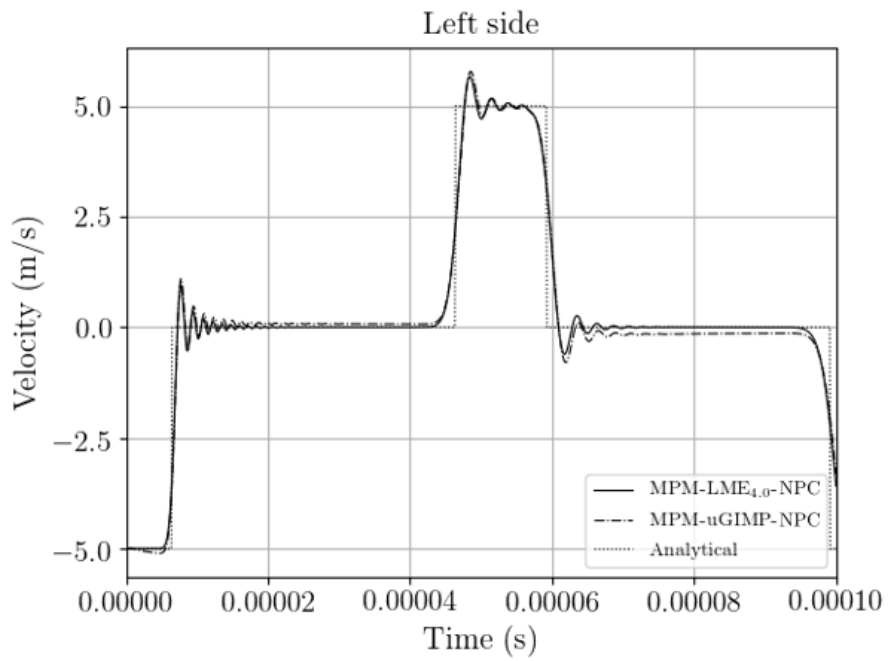


Figure 9: Velocity evolution at the point in the bar left side.

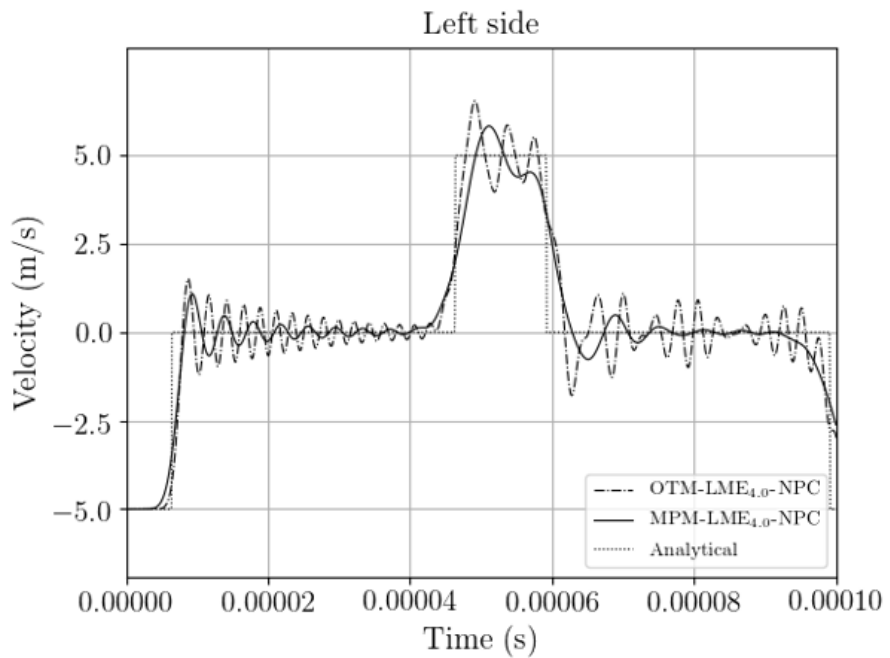


Figure 10: Velocity evolution at the point in the bar left side.

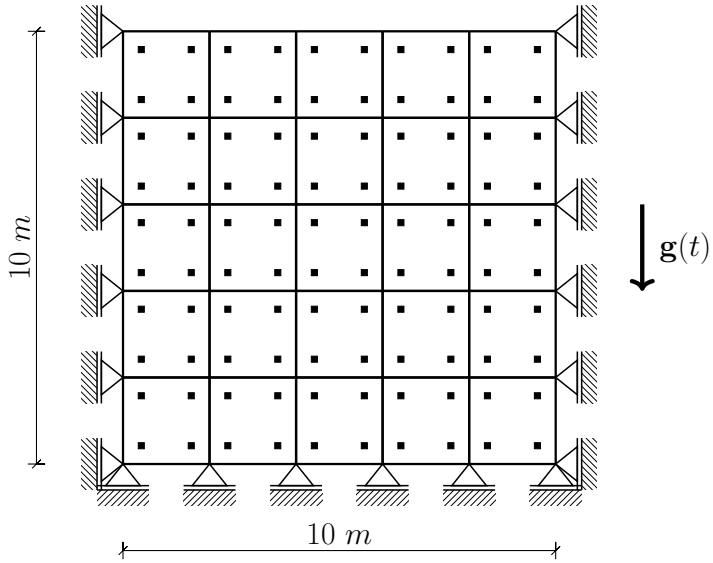


Figure 11: Geometrical description of a soil block

### 3.2. Rigid block

The following test was proposed to validate the ability of the proposed interpolation technique to deal with grid crossing instabilities. A solid elastic square block is incrementally loaded only considering body forces. Details of the problem are sketched in figure 11. This test was previously proposed by Andersen (2009)[34]. The elastic parameters considered for this test are:

- Initial density :  $6 \cdot 10^3 \text{ kg/m}^3$
- Poisson ratio : 0
- Elastic modulus :  $5 \text{ MPa}$

The gravity force is applied as an external force. Using a total time period  $T$  of 20 seconds to apply the gravity, it is increased from 0 to  $9.81\text{m/s}$  with a sinusoidal function until  $T/2$  seconds and then maintained constant until  $T$  in order to reach the equilibrium state:

$$\mathbf{g}(t) = \begin{cases} 0.5\mathbf{g}(\sin(\frac{2t\pi}{T} - \frac{\pi}{2}) + 1) & \text{if } t \leq T/2 \\ \mathbf{g} & \text{if } t > T/2 \end{cases} \quad (45)$$

In order to get a stable solution, time step was conducted by a Courant number of 0.1. The explicit predictor-corrector scheme proposed in previous sections is employed. For the initial spatial discretisation four particles per

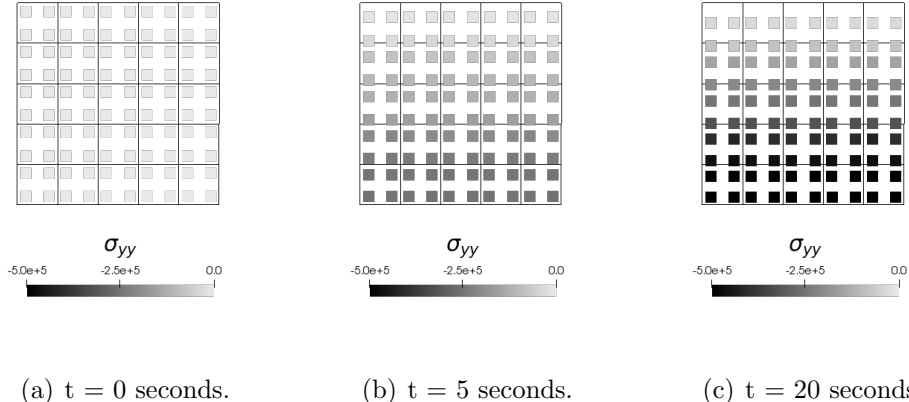


Figure 12: Vertical normal stress and position of material points during the loading process for a soft soil ( $E = 5 \text{ MPa}$ ,  $\rho_0 = 6 \cdot 10^3 \text{ kg/m}^3$ ). Numerical parameters considered for the simulation are : Local *max-ent* shape function  $\hat{\gamma} = 3$  and explicit PC scheme with CFL 0.1.

cell ( $\Delta x = 2 \text{ m}$ ) were adopted. The initial layout of particles inside of the cell changes according to the approximation technique adopted. For the bi-linear shape functions and the LME approximants, the initial position corresponds to the location of the gauss-points in a standard quadratic finite element. For the uGIMP shape function the initial position of each particle is located in the center of each voxel as in the initial situation voxel domains should not overlap.

Figure 12 shows the evolution of the vertical stress during the loading process. The result is physically realistic as the stress increases linearly from the top to the bottom of the specimen, and the value of the vertical stress in a material point located in the bottom of the specimen oscillates around  $5.2 \text{ MPa}$ , which is the analytic value given by  $\sigma_{yy} = \rho g h_y$ .

Figure 13 shows the vertical displacement evolution of a point in the free surface of the block. No results can be appreciated for the MPM simulation with a bi-linear interpolation technique (Q4) as a clear unstable behaviour is observed within the first time steps. The LME simulation was performed using two kinds of shape functions, one with a low value of the dimensionless parameter,  $\hat{\gamma} = 0.8$ , and other with a larger value of it,  $\hat{\gamma} = 3.0$ . Both simulations behave with minimal oscillations and no appreciable differences are observed between them. The uGIMP simulation is more stable than the one performed with the MPM-Q4 and behaves like the LME simulations. Finally, these results are compared against two contrasted techniques. The FEM solution has been done with a regular mesh of linear quadrilaterals, meanwhile the OTM solution has been done with LME approximation. The

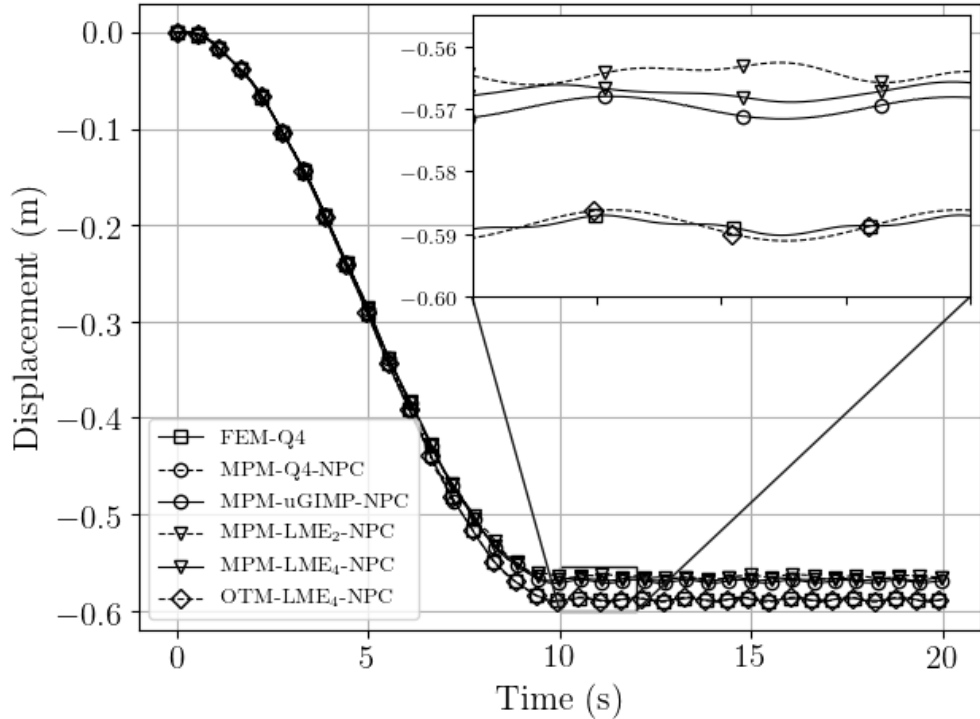


Figure 13: Comparative of the vertical displacement evolution in a point located in the free surface employing different interpolation schemes and numerical techniques.

final displacement in both solutions oscillates around a value of 0.59 m.

### 3.3. 2D elastic wave propagation

This benchmark has been conveniently adapted from the one proposed by Hammerquist & Nairn (2017) [30], it is intended to validate the ability of the discussed time integration schemes in order to reproduce the wave propagation in 2D. The impact of an elastic square plate against a vertical wall is assessed. The square plate dimensions are 50 x 50 m and their elastic parameters are:

- Initial density : 20 kg/m<sup>3</sup>
- Poisson ratio : 0.3
- Elastic modulus : 0.1 MPa

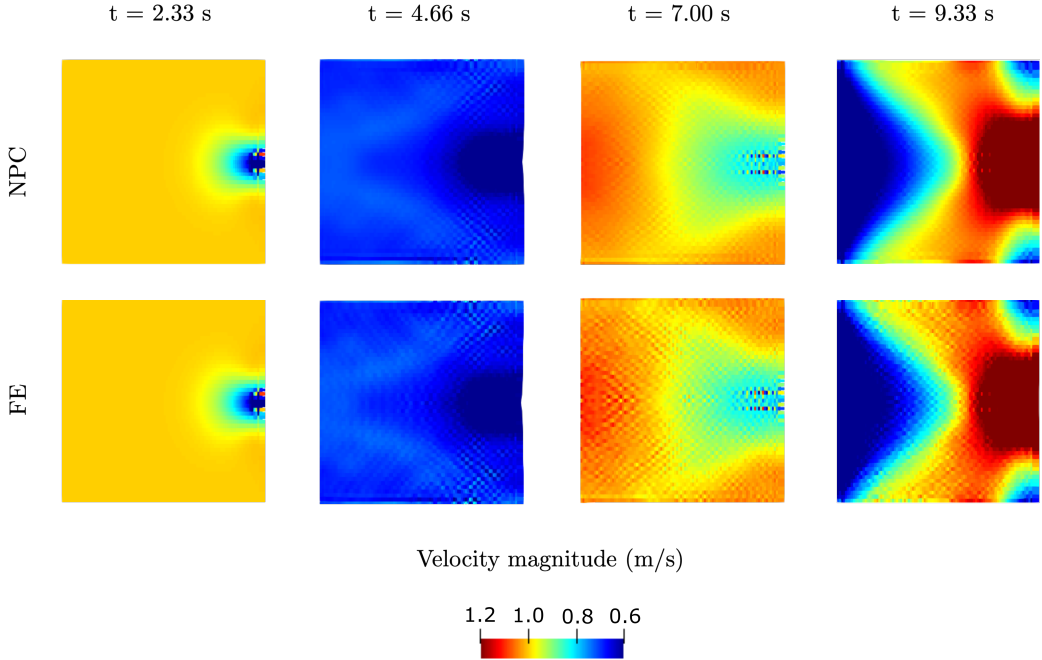


Figure 14: Spatial distribution of the magnitude of the velocity field in an elastic square plate impacted on the right edge. The top row depicts the NPC results meanwhile the bottom row represents the FE ones at different instants.

The background set of nodes is composed by a cartesian grid with an uniform spatial discretisation of 1 m. Four material points per cell are considered. The Courant number is fixed to 0.1 during the whole simulation and LME<sub>3,0</sub> shape functions are employed. A horizontal velocity of the square plate of  $V_0 = 1.0 \text{ m/s}$  is considered until the the plate impacts against the obstacle generating stress waves. The obstacle is modelled as a set of nodes with prescribed velocity equal to zero. Both NPC and FE schemes are compared.

Spatial distribution of the velocity field inside the square plate obtained with both schemes at different times are given in figure 14. At early times, NPC and FE behave in a similar manner. However, at later times, the FE scheme introduces significant numerical noise compared with the NPC one.

Finally, an unstructured background mesh is proposed in order to validate the performance of the LME shape function against the uGIMP one. As it is observed in figure 15, the LME approximation preserves the solution even though the mesh is not structured. Meanwhile, the uGIMP is not able to deal with the unstructured mesh as expected. Thus, the LME approach adopted in the present work shows a remarkable robustness in dealing with unstructured meshes. From this last comparison it can be deduced that

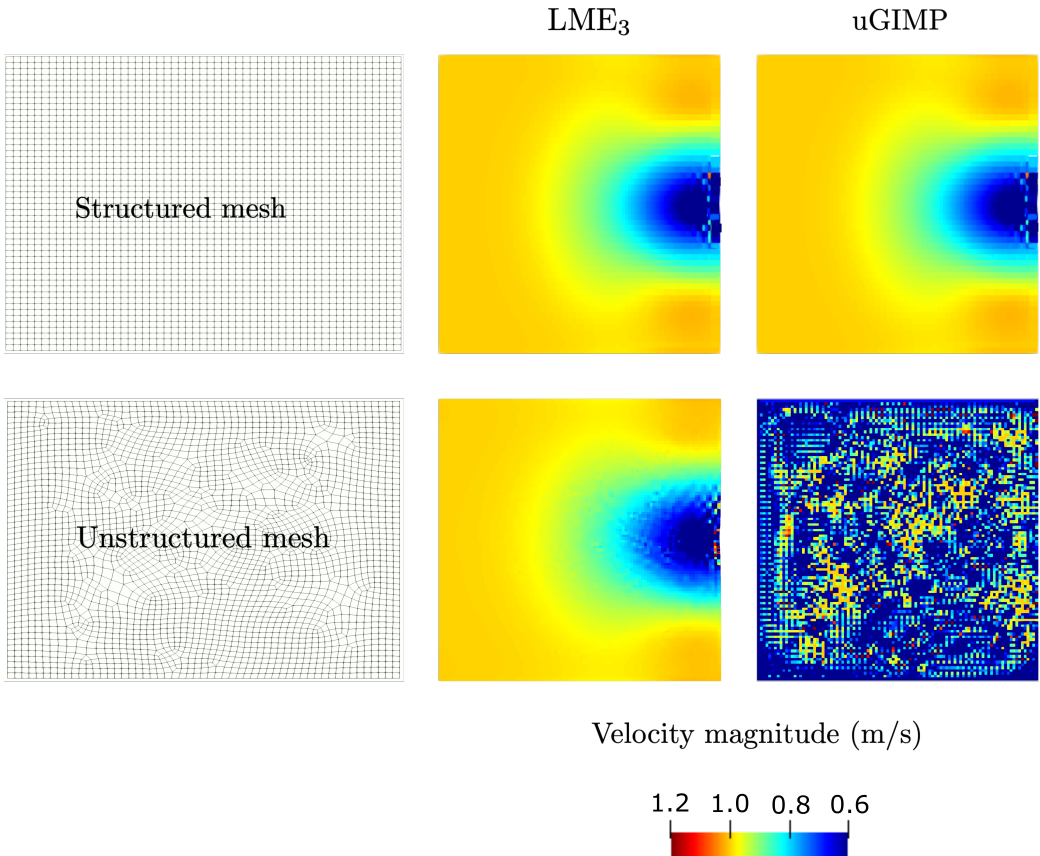


Figure 15: Sensitivity analysis of uGIMP and LME schemes to the randomness in the layout of the background set of nodes. On the left column, sketches of the two employed meshes are depicted. On the right side, spatial distribution of the velocity magnitudes are shown for each case at second 2.66. All the simulation where carried out with the proposed NPC scheme.

LME might be an adequate choice approximation technique when dealing with complex domains where a structured mesh is usually not possible .

#### 4. Conclusions

445 We have proposed in this paper an enhanced methodology which improves Material Point Method (MPM) behaviour in fast dynamic problems. The proposed improvements implemented in the present work are twofold: First, the Newmark Predictor-Corrector (NPC) time integration algorithm to update particles' information, and second, the Local Maximum-Entropy (LME) approximation scheme to define the shape functions. The performance of both  
450 improvements has been assessed with three different benchmarks: Dyka's bar, a solid block under gravity loading and 2D elastic waves propagation.

455 The main achievements of the proposed time discretisation have been observed within Dyka's bar 3.1, where lower error values are obtained compared with the Forward Euler (FE) scheme ones. Furthermore, the NPC approach has shown a more stable performance compared with the FE scheme, being able to dump out spurious numerical oscillations where the FE scheme could not. As per the promising results obtained with the NPC algorithm, the procedure employed in the present work opens the possibility to revisit a huge  
460 variety of time integration schemes developed originally for FEM, which can be implemented within a MPM framework with few modifications. In addition to the implementation of enhanced time integration schemes, further research can be done in the analysis of the good performance of the algorithm within non-linear models, both material and geometric nonlinearity.

465 Regarding the spatial discretisation the Local Maximum-Entropy (LME) approximation scheme has been validated as a robust and versatile tool in the MPM framework. It also comes up as a promising alternative to other approximation techniques, developed within the MPM framework, in order to overcome grid crossing limitations and to avoid the constriction of the  
470 uGIMP of a regular mesh or a high density of particles per cell as it was observed in section 3.3. Several research lines of the LME scheme dive into the improvement of the methodology, focusing in the optimization of the calculation of the shape function and the possibility of adapting the parameter  $\beta(\vec{x})$  through the deformation gradient in order to align the shape functions in the principal strain direction to select the most suitable set of nodes adapted to the strain. Another possibility could be to adapt the value of  $\beta$  to solve the equations FEM-like or meshfree-like depending on the behaviour of the region. Together with the implementation of non-linear behaviours, previously mentioned, challenging scenarios could be reproduced, being the main  
475

- 480 purpose of the research line the simultaneous simulation of both initialization and propagation stages of fast landslides.

### Conflict of interest

The authors declare that they have no conflict of interest.

### Acknowledgements

- 485 The financial support to develop this research from the Ministerio de Ciencia e Innovación, under Grant No. BIA-2016-76253 is greatly appreciated. The first and the second authors also acknowledge the fellowship Fundación Agustín de Betancourt and Juan de la Cierva (FJCI-2017-31544) respectively.

490 **Appendix A. The analytical solution of the 1D Dyka benchmark**

For the derivation of this analytical solution, a 1D elastic bar is considered. Henceforth for convenience the governing equations will be written in terms of stress and velocity. The balance of linear momentum,

$$\rho \frac{\partial v}{\partial t} = \frac{\partial \sigma}{\partial x}, \quad (\text{A.1})$$

Secondly the constitutive equation is the well known linear elastic one,

$$\frac{\partial \sigma}{\partial t} = E \frac{\partial \varepsilon}{\partial t}, \quad (\text{A.2})$$

where  $E$  is the elastic modulus. And finally the compatibility equation,

$$\frac{\partial \varepsilon}{\partial t} = \frac{\partial v}{\partial x}. \quad (\text{A.3})$$

Next for simplicity, we will introduce (A.3) in (A.2), it yield to,

$$\frac{\partial v}{\partial t} = \frac{1}{\rho} \frac{\partial \sigma}{\partial x}, \quad (\text{A.4})$$

$$\frac{\partial \sigma}{\partial t} = E \frac{\partial v}{\partial x}. \quad (\text{A.5})$$

Introducing (A.5) in (A.4) and expressing the remaining equation in terms of the displacement, results the wave equation for linear elastic materials,

$$\frac{\partial^2 u}{\partial t^2} = \frac{E}{\rho} \frac{\partial^2 u}{\partial x^2} = c^2 \frac{\partial^2 u}{\partial x^2} \quad (\text{A.6})$$

where  $c = \sqrt{\frac{E}{\rho}}$  is the material celerity. Alternative, rearranging both equations (A.4) and (A.5) it is possible to join them in a single system of equations as,

$$\frac{\partial}{\partial t} \begin{bmatrix} \sigma \\ v \end{bmatrix} + \begin{bmatrix} 0 & -E \\ -1/\rho & 0 \end{bmatrix} \begin{bmatrix} \frac{\partial \sigma}{\partial x} \\ \frac{\partial v}{\partial x} \end{bmatrix} = \mathbf{0}. \quad (\text{A.7})$$

Or in a more compact format,

$$\frac{\partial \phi}{\partial t} + \mathbf{A} \frac{\partial \phi}{\partial x} = \mathbf{0}. \quad (\text{A.8})$$

In (A.8) stress and velocity are joined in to a single structure  $\phi$  and  $\mathbf{A}$  in coupling matrix between both equations,

$$\phi = \begin{bmatrix} \sigma \\ v \end{bmatrix}, \quad \mathbf{A} = \begin{bmatrix} 0 & -E \\ -1/\rho & 0 \end{bmatrix}.$$

Despite of this manipulation, the nature of is still hyperbolic. A proof of this can be easily obtained computing the zeros of the hypersurface defined by (A.6). And later the eigenvalues of  $\mathbf{A}$  in (A.8). In both cases, eigenvalues are real and distinct ( $\lambda = \pm \sqrt{\frac{E}{\rho}}$ ), therefore the system is called strictly hyperbolic. Assuming that  $\mathbf{A}$  has  $n$  different eigenvalues  $\{\lambda_1, \dots, \lambda_i, \dots, \lambda_n\}$  and  $n$  eigenvectors  $\{\vec{x}^1, \dots, \vec{x}^i, \dots, \vec{x}^n\}$  satisfying that  $\mathbf{A}\vec{x} = \lambda\vec{x}$ . Now we introduce the matrix  $\mathbf{P}$  whose columns are the  $n$  eigenvalues  $\mathbf{x}$

$$\mathbf{P} = \{\vec{x}^1, \vec{x}^2, \vec{x}^3, \dots, \vec{x}^n\}. \quad (\text{A.9})$$

Diagonalizing  $\mathbf{A}$  using  $\mathbf{P}$  yields,

$$\Lambda = \mathbf{P}^{-1} \mathbf{A} \mathbf{P}, \quad (\text{A.10})$$

where  $\Lambda_{ii} = \lambda_i$ . Now, lets define a vector  $\mathfrak{R}$  as

$$\phi = \mathbf{P} \mathfrak{R}. \quad (\text{A.11})$$

Expanding the above expression with the chain rule and passing the matrix  $\mathbf{P}$  to left hand side of the equality we get,

$$d\vec{\mathfrak{R}} = \frac{\partial \mathfrak{R}}{\partial t} dt + \frac{\partial \mathfrak{R}}{\partial x} dx = \mathbf{P}^{-1} \left( \frac{\partial \phi}{\partial t} dt + \frac{\partial \phi}{\partial x} dx \right) \quad (\text{A.12})$$

and setting the terms we get,

$$\frac{\partial \Re}{\partial t} = \mathbf{P}^{-1} \frac{\partial \phi}{\partial t}, \quad \frac{\partial \Re}{\partial x} = \mathbf{P}^{-1} \frac{\partial \phi}{\partial x} \quad (\text{A.13})$$

Next, if we multiply (A.8) by  $\mathbf{P}^{-1}$  we get:

$$\mathbf{P}^{-1} \frac{\partial \phi}{\partial t} + (\mathbf{P}^{-1} \mathbf{A} \mathbf{P}) \mathbf{P}^{-1} \frac{\partial \phi}{\partial x} = \mathbf{0} \quad (\text{A.14})$$

finally introducing the expressions (A.13) we reach to

$$\frac{\partial \Re}{\partial t} + \Lambda \frac{\partial \Re}{\partial x} = \mathbf{0} \quad (\text{A.15})$$

which consists of  $n$  uncoupled equations as  $\Lambda$  is diagonal matrix as we can see in (A.10). Each of this equations are 1D scalar convective transport equations, with solutions of the form:

$$\Re^{(i)} = F^{(i)} (x - \lambda^{(i)} t) \quad (\text{A.16})$$

This uncoupled system, has a set of  $n$  characteristics. These magnitudes  $\Re_i$  which propagate along characteristics are known as *Riemann invariants* of the problem. For the closure of the problem it is required “n” initial conditions of the form  $\Re_i(x, t = 0) = h_i(x)$ , and “n” boundary conditions. Particularizing the previous equations for the 1D elastic bar described in [46],  $\mathbf{P}$  can be computed as,

$$\mathbf{P} = \begin{bmatrix} -\sqrt{E\rho} & \sqrt{E\rho} \\ 1 & 1 \end{bmatrix}$$

With the value of the inverse matrix  $\mathbf{P}^{-1}$  in the Riemann definition (A.11), a set of equations arise,

$$\Re^I = \frac{1}{2\sqrt{\rho E}} (-\sigma + v \sqrt{\rho E}) \quad (\text{A.17})$$

$$\Re^{II} = \frac{1}{2\sqrt{\rho E}} (\sigma + v \sqrt{\rho E}) \quad (\text{A.18})$$

From (A.17) and (A.18) the values of the stress and the velocity can be computed in the following way,

$$v = \Re^I + \Re^{II} , \quad \sigma = \sqrt{E\rho} (\Re^{II} - \Re^I) \quad (\text{A.19})$$

The boundary conditions are in both cases of radiation as there is not wave in-going from the exterior. So for the right side the conditions are,

$$\Re^{II} = 0 \quad \text{and} \quad v_{x=L} = 0 \quad \Rightarrow \quad \sigma_{x=L} = -2\sqrt{\rho E} \Re^I$$

And in the left side,

$$\Re^I = 0 \quad \text{and} \quad \sigma_{x=0} = 0 \quad \Rightarrow \quad v_{x=0} = 2\Re^{II}$$

By imposing this boundary conditions, the problem is fully defined as in [46].

## References

- [1] D. L. Sulsky, H. Schreyer, Z. Chen, A particle method for history-dependent materials, Computer Methods in Applied Mechanics and Engineering 118 (1) (1994) 179–196. doi:10.1016/0045-7825(94)90112-0.
- [2] J. U. Brackbill, H. M. Ruppel, FLIP: A method for adaptively zoned, particle-in-cell calculations of fluid flows in two dimensions, Journal of Computational Physicsdoi:10.1016/0021-9991(86)90211-1.
- [3] S. G. S. G. Bardenhagen, E. M. Kober, The generalized interpolation material point method, CMES - Computer Modeling in Engineering and Sciences 5 (6) (2004) 477–495.
- [4] M. Steffen, R. M. Kirby, M. Berzins, Analysis and reduction of quadrature errors in the material point method (MPM), International Journal for Numerical Methods in Engineering 76 (6) (2008) 922–948. doi:10.1002/nme.2360.  
URL <http://doi.wiley.com/10.1002/nme.2360>
- [5] D. Z. Zhang, X. Ma, P. T. Giguere, Material point method enhanced by modified gradient of shape function, Journal of Computational Physics 230 (16) (2011) 6379–6398. doi:10.1016/J.JCP.2011.04.032.  
URL <https://www.sciencedirect.com/science/article/pii/S0021999111002804>
- [6] T. R. Dhakal, D. Z. Zhang, Material point methods applied to one-dimensional shock waves and dual domain material point method with sub-points, Journal of Computational Physics 325 (2016) 301 – 313. doi:<https://doi.org/10.1016/j.jcp.2016.08.033>.  
URL <http://www.sciencedirect.com/science/article/pii/S0021999116303904>
- [7] A. Sadeghirad, R. M. Brannon, J. Burghardt, A convected particle domain interpolation technique to extend applicability of the material point method for problems involving massive deformations, International Journal for Numerical Methods in Engineering 86 (12) (2011) 1435–1456. arXiv:<https://onlinelibrary.wiley.com/doi/pdf/10.1002/nme.3110>. doi:10.1002/nme.3110.  
URL <https://onlinelibrary.wiley.com/doi/abs/10.1002/nme.3110>

- 530 [8] R. Tielen, E. Wobbes, M. Möller, L. Beuth, A high order material point method, *Procedia Engineering* 175 (2017) 265 – 272, proceedings of the 1st International Conference on the Material Point Method (MPM 2017). doi:<https://doi.org/10.1016/j.proeng.2017.01.022>.  
URL <http://www.sciencedirect.com/science/article/pii/S187770581730022X>
- 535 [9] E. Wobbes, M. Moller, V. Galavi, C. Vuik, M. Möller, V. Galavi, C. Vuik, M. Moller, V. Galavi, C. Vuik, Conservative Taylor Least Squares reconstruction with application to material point methods: Conservative Taylor Least Squares reconstruction, *International Journal for Numerical Methods in Engineering* 117 (3) (2018) 271–290. doi:[10.1002/nme.5956](https://doi.org/10.1002/nme.5956).
- 540 [10] M. Arroyo, M. Ortiz, Local maximum-entropy approximation schemes: A seamless bridge between finite elements and meshfree methods, *International Journal for Numerical Methods in Engineering* doi:[10.1002/nme.1534](https://doi.org/10.1002/nme.1534).
- 545 [11] D. Millán, N. Sukumar, M. Arroyo, Cell-based maximum-entropy approximants, *Comput. Meth. Appl. Mech. Engrg.* 284 (2015) 712–731.
- [12] B. Li, A. Kidane, G. Ravichandran, M. Ortiz, Verification and validation of the Optimal Transportation Meshfree (OTM) simulation of terminal ballistics, *International Journal of Impact Engineering* doi:[10.1016/j.ijimpeng.2011.11.003](https://doi.org/10.1016/j.ijimpeng.2011.11.003).
- 550 [13] P. Navas, L. Sanavia, S. López-Querol, R. C. Yu, Explicit mesh-free solution for large deformation dynamic problems in saturated porous media., *Acta geotechnica* 13 (2018) 227–242. doi:[10.1007/s11440-017-0612-7](https://doi.org/10.1007/s11440-017-0612-7).
- 555 [14] P. Navas, S. López-Querol, R. C. Yu, M. Pastor, Optimal transportation meshfree method in geotechnical engineering problems under large deformation regime, *International Journal for Numerical Methods in Engineering* doi:[10.1002/nme.5841](https://doi.org/10.1002/nme.5841).
- 560 [15] P. Navas, S. López-Querol, R. C. Yu, B. Li, B-bar based algorithm applied to meshfree numerical schemes to solve unconfined seepage problems through porous media, *Int. J. Numer. Anal. Methods Geomech.* 40 (6) (2016) 962–984. doi:[10.1002/nag.2472](https://doi.org/10.1002/nag.2472).
- [16] P. Navas, R. C. Yu, S. López-Querol, B. Li, Dynamic consolidation problems in saturated soils solved through u-w formulation in a LME

- meshfree framework, *Comput. Geotech.* 79 (2016) 55–72. doi:10.1016/j.compgeo.2016.05.021.
- 565 [17] P. Navas, L. Sanavia, S. López-Querol, R. C. Yu, u-w formulation for dynamic problems in large deformation regime solved through an implicit meshfree scheme., *Comput. Mech.* 62 (2018) 745–760. doi:10.1007/s00466-017-1524-y.
- 570 [18] C. Weißenfels, P. Wriggers, Stabilization algorithm for the optimal transportation meshfree approximation scheme, *Comput. Meth. Appl. Mech. Engrg.* 329 (2018) 421–443.
- [19] E. Wobbes, R. Tielen, M. Möller, C. Vuik, Comparison and unification of material-point and optimal transportation meshfree methods, *Computational Particle Mechanics* doi:10.1007/s40571-020-00316-7.
- 575 [20] Q. A. Tran, W. Sołowski, Temporal and null-space filter for the material point method, *International Journal for Numerical Methods in Engineering* doi:10.1002/nme.6138.
- 580 [21] J. Guilkey, J. Weiss, Implicit time integration for the material point method: Quantitative and algorithmic comparisons with the finite element method, *International Journal for Numerical Methods in Engineering* 57 (2003) 1323 – 1338. doi:10.1002/nme.729.
- [22] B. Wang, P. Vardon, M. Hicks, Z. Chen, Development of an implicit material point method for geotechnical applications, *Computers and Geotechnics* 71 (2016) 159–167. doi:10.1016/j.compgeo.2015.08.008.
- 585 [23] T. J. Charlton, W. M. Coombs, C. E. Augarde, iGIMP: An implicit generalised interpolation material point method for large deformations, *Computers & Structures* 190 (2017) 108–125. doi:10.1016/j.compstruc.2017.05.004.
- 590 [24] S. Kularathna, K. Soga, Implicit formulation of material point method for analysis of incompressible materials, *Computer Methods in Applied Mechanics and Engineering* 313 (2017) 673 – 686. doi:<https://doi.org/10.1016/j.cma.2016.10.013>.  
 URL <http://www.sciencedirect.com/science/article/pii/S0045782516313081>

- [25] M. Lu, J. Zhang, H. Zhang, Y. Zheng, Z. Chen, Time-discontinuous material point method for transient problems, Computer Methods in Applied Mechanics and Engineering 328 (2018) 663 – 685. doi:<https://doi.org/10.1016/j.cma.2017.09.022>.  
600 URL <http://www.sciencedirect.com/science/article/pii/S0045782517301779>
- [26] E. L. Wilson, I. Farhoomand, K. J. Bathe, Nonlinear dynamic analysis of complex structures, Earthquake Engineering & Structural Dynamics 1 (3) (1972) 241–252. doi:[10.1002/eqe.4290010305](https://doi.org/10.1002/eqe.4290010305).  
605 URL <http://doi.wiley.com/10.1002/eqe.4290010305>
- [27] J. Chung, G. M. Hulbert, A Time Integration Algorithm for Structural Dynamics With Improved Numerical Dissipation: The Generalized-alpha Method, J. Appl. Mech. 60 (2) (1993) 371. doi:[10.1115/1.2900803](https://doi.org/10.1115/1.2900803).
- 610 [28] J. Brackbill, The ringing instability in particle-in-cell calculations of low-speed flow, Journal of Computational Physics 75 (2) (1988) 469 – 492. doi:[https://doi.org/10.1016/0021-9991\(88\)90123-4](https://doi.org/10.1016/0021-9991(88)90123-4).  
URL <http://www.sciencedirect.com/science/article/pii/0021999188901234>
- 615 [29] C. Gritton, M. Berzins, Improving accuracy in the MPM method using a null space filter, Computational Particle Mechanics doi:[10.1007/s40571-016-0134-3](https://doi.org/10.1007/s40571-016-0134-3).
- [30] C. C. Hammerquist, J. A. Nairn, A new method for material point method particle updates that reduces noise and enhances stability, Computer Methods in Applied Mechanics and Engineering 318 (2017) 724 – 738. doi:<https://doi.org/10.1016/j.cma.2017.01.035>.  
620 URL <http://www.sciencedirect.com/science/article/pii/S004578251631547X>
- 625 [31] B. Riemann, Über die darstellbarkeit einer function durch eine trigonometrische reihe, Abhandlungen der Königlichen Gesellschaft der Wissenschaften zu Göttingen 13 (1854) 87 – 138. doi:<https://doi.org/10.1016/j.cma.2017.09.022>.
- [32] X. Zhang, Z. Chen, Y. Liu, The Material Point Method: A Continuum-Based Particle Method for Extreme Loading Cases, Elsevier, 2016. doi:[10.1016/b978-0-12-407716-4.00003-x](https://doi.org/10.1016/b978-0-12-407716-4.00003-x).  
630

- [33] S. G. S. Bardenhagen, Energy Conservation Error in the Material Point Method for Solid Mechanics, *Journal of Computational Physics* 180 (1) (2002) 383–403. doi:10.1006/JCPH.2002.7103.
- [34] S. M. Andersen, Material-Point Analysis of Large-Strain Problems: modelling of landslides, Ph.D. thesis, Department of Civil Engineering, Aalborg University (2009).
- [35] T. J. R. Hughes, *The finite element method : linear static and dynamic finite element analysis*, Dover Publications, 2000.
- [36] X. Liu, On the stability of a newmark's scheme-based predictor-corrector algorithm, *Computers & Structures* 53 (1994) 27–33. doi:10.1016/0045-7949(94)90126-0.
- [37] O. C. Zienkiewicz, J. Z. Zhu, The superconvergent patch recovery and a posteriori error estimates. part 1: The recovery technique, *International Journal for Numerical Methods in Engineering* 33 (7) (1992) 1331–1364. doi:10.1002/nme.1620330702.
- [38] Z. Więckowski, The material point method in large strain engineering problems, *Computer Methods in Applied Mechanics and Engineering* 193 (39-41 SPEC. ISS.) (2004) 4417–4438. doi:10.1016/j.cma.2004.01.035.
- [39] E. Jaynes, Information Theory and Statistical Mechanics, *The Physical Review* 106 (4) (1957) 620–630.
- [40] M. Steffen, P. C. Wallstedt, J. Guilkey, R. M. Kirby, M. Berzins, Examination and analysis of implementation choices within the Material Point Method (MPM), *CMES - Computer Modeling in Engineering and Sciences* 31 (2) (2008) 107–127.
- [41] G. R. G.-R. Liu, M. B. Liu, *Smoothed particle hydrodynamics : a meshfree particle method*, World Scientific, 2003.  
URL [https://books.google.es/books/about/Smoothed\\_{\\\_}Particle\\_{\\\_}Hydrodynamics.html?id={\\\_}cwFMmEQvZQC{&}redir\\_{\\\_}esc=y](https://books.google.es/books/about/Smoothed_{\_}Particle_{\_}Hydrodynamics.html?id={\_}cwFMmEQvZQC{&}redir_{\_}esc=y)
- [42] Z. Ullah, W. Coombs, C. Augarde, An adaptive finite element/meshless coupled method based on local maximum entropy shape functions for linear and nonlinear problems, *Computer Methods in Applied Mechanics and Engineering* 267 (2013) 111 – 132. doi:<https://doi.org/10.1016/j.cma.2013.07.018>.

- URL <http://www.sciencedirect.com/science/article/pii/S0045782513001941>
- [43] W.-C. Yang, P. Arduino, G. R. Miller, P. Mackenzie-Helnwein, Smoothing algorithm for stabilization of the material point method for fluid–solid interaction problems, Computer Methods in Applied Mechanics and Engineering 342 (2018) 177 – 199. doi:<https://doi.org/10.1016/j.cma.2018.04.041>.  
URL <http://www.sciencedirect.com/science/article/pii/S0045782518302263>
- [44] S. Kumar, K. Danas, D. M. Kochmann, Enhanced local maximum-entropy approximation for stable meshfree simulations, Computer Methods in Applied Mechanics and Engineering doi:[10.1016/j.cma.2018.10.030](https://doi.org/10.1016/j.cma.2018.10.030).
- [45] M. Cortis, W. Coombs, C. Augarde, M. Brown, A. Brennan, S. Robinson, Imposition of essential boundary conditions in the material point method, International Journal for Numerical Methods in Engineering 113 (1) (2018) 130–152. doi:[10.1002/nme.5606](https://doi.org/10.1002/nme.5606).  
URL <http://doi.wiley.com/10.1002/nme.5606>
- [46] C. Dyka, R. Ingel, An approach for tension instability in smoothed particle hydrodynamics (SPH), Computers & Structures 57 (4) (1995) 573–580. doi:[10.1016/0045-7949\(95\)00059-P](https://doi.org/10.1016/0045-7949(95)00059-P).
- [47] B. Li, F. Habbal, M. Ortiz, Optimal transportation meshfree approximation schemes for fluid and plastic flows, International Journal for Numerical Methods in Engineering 83 (12) (2010) 1541–1579. doi:[10.1002/nme.2869](https://doi.org/10.1002/nme.2869).  
URL <http://doi.wiley.com/10.1002/nme.2869>